

STUDY OF CFD VARIATION ON TRANSPORT CONFIGURATIONS FROM THE SECOND DRAG-PREDICTION WORKSHOP

Christopher L. Rumsey,* S. Melissa Rivers,[†] and Joseph H. Morrison[‡]
NASA Langley Research Center
Hampton, Virginia

Abstract

This paper describes and analyzes a series of nearly 90 CFD test cases performed as a contribution to the second Drag Prediction Workshop, held in association with the AIAA in June 2003. Two configurations are included: DLR-F6 wing-body and wing-body-nacelle-pylon. The ability of CFD to predict the drag, lift, and pitching moment from experiment – including the “delta” arising from the addition of the nacelle and pylon – is assessed. In general, at a fixed angle of attack CFD overpredicts lift, but predicts the ΔC_L reasonably well. At low lift levels ($C_L < 0.3$), ΔC_D is 20–30 drag counts (30–45%) high. At the target lift coefficient of $C_L = 0.5$, ΔC_D is overpredicted by between 11–16 counts. However, the primary contribution of this paper is not so much the assessment of CFD against experiment, but rather a detailed assessment and analysis of CFD variation. The series of test cases are designed to determine the sensitivity/variability of CFD to a variety of factors, including grid, turbulence model, transition, code, and viscous model. Using medium-level grids (6–11 million points) at the target lift coefficient, the maximum variation in drag due to different grids is 5–11 drag counts, due to code is 5–10 counts, due to turbulence model is 7–15 counts, due to transition is 10–11 counts, and due to viscous model is 4–5 counts. Other specific variations are described in the paper.

1 Introduction

Drag prediction to the level of accuracy desired by airframe manufacturers is currently not possible with CFD. Grid resolution and numerical accuracy, as well as transition and turbulence modeling

issues cause uncertainty and prevent confident assessments. It is therefore important to routinely examine CFD capabilities in this area by methodically assessing the influence of various numerical parameters and physical models.

A Drag Prediction Workshop (DPW-I) was held in June 2001 to determine the numerical variation on a simple wing-body configuration (DLR-F4).¹ Several papers were written assessing the overall results of that workshop,^{2,3} including statistical analysis. DPW-I results involving the current authors were also summarized.^{4,5} A second Drag Prediction Workshop (DPW-II) was held in June 2003 for the generic DLR-F6 configuration,⁶ both as a wing-body alone (WB) as well as wing-body with nacelle-pylon (WBNP). The current paper summarizes a contribution to this effort with two CFD codes widely used in the U.S. aerospace industry: OVERFLOW and CFL3D.

OVERFLOW^{7,8} is an overset (Chimera), structured grid Navier-Stokes flow solver based on the finite difference method. It can be run using second-order central differencing or third-order upwind differencing with flux difference-splitting (FDS). For all results in this study, FDS was used. OVERFLOW is advanced in time with first-order implicit time advancement. It was developed at NASA for multiple/moving body transonic aerodynamics problems, and has been used for a wide variety of geometries and flow regimes, from low subsonic through hypersonic speeds.^{9,10}

CFL3D¹¹ is a finite volume method that has also been used extensively for complex aerospace applications. It uses third-order upwind-biased spatial differencing on the convective and pressure terms, and second-order differencing on the viscous terms; it is globally second-order spatially accurate. FDS is employed to obtain fluxes at the cell faces. It is advanced in time with an implicit three-factor approximate factorization method.

For this DPW-II study, required single point (fixed C_L) and drag polar cases were run using two different supplied grid systems for both the WB and

*Research Scientist, Computational Modeling and Simulation Branch, Associate Fellow AIAA.

[†]Aerospace Engineer, Configuration Aerodynamics Branch, Member AIAA.

[‡]Research Scientist, Computational Modeling and Simulation Branch, Senior member AIAA.

This material is declared a work of the U.S. Government and is not subject to copyright protection in the United States.

WBNP configurations. The effect of grid was investigated, and flow solver options evaluated included turbulence model choice, free transition (“fully turbulent”) vs. specified transition, code, and viscous model (thin-layer in one direction vs. thin-layer in three directions vs. full Navier-Stokes).

The choice of turbulence model typically has less effect on aerodynamic forces in the attached flow regimes that characterize cruise than at off-design conditions in the presence of flow separation. Although the lift coefficient values for the DPW-II workshop cases were below buffet, there was evidence of separated regions in the experiment. Therefore, the behavior of three different turbulence models was examined and documented. These models included the one-equation Spalart-Allmaras (SA),¹² two-equation Menter shear-stress transport (SST),¹³ and two-equation explicit algebraic stress in k-omega form (EASM-ko).^{14,15}

This paper is organized as follows. Section 2 briefly outlines key points from the numerical methods and turbulence models of the two codes, then section 3 summarizes the computations performed for this study. Results are given in section 4, and summary and conclusions are made in section 5.

2 Computational Approach

2.1 Numerical Methods

Details concerning the equations and numerical methods in OVERFLOW⁷⁻¹⁰ and CFL3D¹¹ are given in their respective references. Here, we briefly point out some of the key issues relevant to the current study.

The Navier-Stokes equations can be written in vector form for an arbitrary coordinate system (ξ, η, ζ) as:

$$\frac{\partial \hat{Q}}{\partial t} + \frac{\partial(\hat{F} - \hat{F}_v)}{\partial \xi} + \frac{\partial(\hat{G} - \hat{G}_v)}{\partial \eta} + \frac{\partial(\hat{H} - \hat{H}_v)}{\partial \zeta} = 0 \quad (1)$$

where \hat{Q} is the vector of conserved variables $\hat{Q} = [\rho, \rho u, \rho v, \rho w, \rho E]/J$, and J is the metric Jacobian, ρ is density, u, v, w are the velocity components, and E is the total energy. Terms are nondimensionalized by freestream density, freestream speed of sound, freestream molecular viscosity, and a reference length L . The \hat{F}, \hat{G} , and \hat{H} terms represent inviscid fluxes, and \hat{F}_v, \hat{G}_v , and \hat{H}_v terms represent viscous fluxes (including turbulence effects). These expressions are not given here, but can be found, for example, in Krist et al.¹¹ The viscous fluxes are made up of terms involving derivatives of the shear

stress and viscous heat flux:

$$\tau_{ij} = (\mu + \mu_T) \frac{M_\infty}{Re} \left[\left(\frac{\partial u_i}{\partial x_j} + \frac{\partial u_j}{\partial x_i} \right) - \frac{2}{3} \frac{\partial u_k}{\partial x_k} \delta_{ij} \right] \quad (2)$$

$$\dot{q}_i = -\frac{M_\infty}{Re(\gamma - 1)} \left(\frac{\mu}{Pr} + \frac{\mu_T}{Pr_T} \right) \frac{\partial a^2}{\partial x_i} \quad (3)$$

where the eddy viscosity term μ_T has been included; it brings in the turbulence effects for linear eddy-viscosity turbulence models. Note that the viscous heat flux has been written using the gradient of local speed of sound (a) squared, rather than gradient of temperature.

For full Navier-Stokes, the viscous fluxes are expanded in the (ξ, η, ζ) coordinate system via the chain rule, and all terms are retained. For the thin-layer approximation in three directions, all cross-derivative terms (e.g., $\partial/\partial\xi[\partial()/\partial\eta]$) are neglected. For the thin-layer approximation in one direction (the body-normal direction), all cross-derivative terms are neglected *and* all viscous terms in the two coordinate directions parallel to solid walls are also neglected. The assumption of thin-layer in the body-normal direction is often reasonable for high Reynolds number aerodynamic flows, because typically only the shear stress and heat flux derivatives normal to solid walls are significant. Also, often the grid resolution in directions parallel to solid walls is insufficient to adequately resolve the viscous terms.

CFL3D has the capability for thin-layer in one, two, or three coordinate directions, but not full Navier-Stokes. OVERFLOW has the capability for any of the approximations including full Navier-Stokes. Typically, most users of both codes utilize thin-layer in the body-normal direction for high Reynolds number aerodynamic flows, although this general practice may be changing. Note, however, that to utilize this approximation in CFL3D, the same coordinate direction (ξ , for example) must be the body-normal direction everywhere in the grid. This was not true in the 1-to-1 grids used in this study, so thin-layer in all three coordinate directions had to be used with CFL3D in these cases.

2.2 Turbulence Models

A brief summary of the turbulence models is now given. The complete equations can be found in their respective references. The SA model is a widely-used one-equation model for a term related to the eddy viscosity. There are several versions with minor variations in use today. CFL3D employs the version of the model that is given in Spalart and Allmaras.¹² In its default mode of operation, OVERFLOW employs a modification to the SA model that is un-

published: it employs an additional term f_{v3} that multiplies part of the source term (see Rumsey et al.¹⁶ for details). However, for all the cases run in this study, the same SA model¹² was used in both codes.

The SST model is a two-equation model for k and ω that represents a blend between more traditional k - ϵ and k - ω models. It also contains a limiter that allows the model to account for the transport of the principal shear stress in adverse pressure gradient boundary layers.

Both SA and SST are linear eddy viscosity models. The third model employed in the current study, EASM-ko, is a nonlinear eddy viscosity model. Like SST, EASM-ko obtains an eddy viscosity μ_T by solving two transport equations for k and ω . This model is derived directly from the full Reynolds stress equations, by making simplifying assumptions.^{17,18} The end result is that the eddy viscosity is derived as

$$\mu_T = C_\mu^* \frac{\rho k}{\omega} \quad (4)$$

where C_μ^* is a variable rather than the usual constant. The nonlinear terms come in as additional terms that are added to Eq. 2. These nonlinear terms are functions of combinations of S_{ij} and W_{ij} , where $S_{ij} = (\partial u_i / \partial x_j + \partial u_j / \partial x_i) / 2$ is the strain rate tensor and $W_{ij} = (\partial u_i / \partial x_j - \partial u_j / \partial x_i) / 2$ is the rotation rate tensor. Nonlinear terms are known to be important for computing certain flows such as corner-flow in a square duct (where the corner recirculation is driven by turbulent stress differences), but it has not yet been demonstrated how important they are for aircraft configurations. EASM-ko is available in CFL3D, but not in OVERFLOW.

3 Computations Performed

Tables 1, 2, and 3 detail the nearly 90 computations performed for the current effort, whose combined purpose was to study: (1) grid effects using the same code and turbulence model, (2) turbulence model effects using the same grid and code, (3) transition location effects using the same grid, code and turbulence model, (4) the effect of code (OVERFLOW compared to CFL3D) using the same grid and turbulence model, and (5) viscous modeling effects using the same grid, code, and turbulence model. In Table 1, note that case 1.16 (CFL3D on the overset grid for WBNP(f)) was planned, but was not run due to resource constraints.

In these tables, “C-1to1” stands for CFL3D using a 1-to-1 (point-matched) grid, “C-overset” stands for CFL3D using an overset grid, and “O-overset” stands for OVERFLOW using an overset grid. For

the viscous model, “t1” stands for thin-layer in one direction (the direction normal to the body surface), “t3” stands for thin-layer in all three grid coordinate directions, and “full” stands for full Navier-Stokes. For the case designations, “WB” stands for wing-body configuration, “WBNP” stands for wing-body-nacelle-pylon, “(c)” stands for coarse grid, “(m)” stands for medium, and “(f)” stands for fine. When the codes were run “fully turbulent,” the turbulence was allowed to develop everywhere (i.e., the turbulence model transitioned on its own). When the codes were run “transition specified,” the production terms in the turbulence models were turned off in specific regions where laminar flow was desired. In order to approximately match experimentally-observed transition locations, these designated regions were as follows: (1) 25% of the local chord on the wing lower surface; (2) variable location on the upper surface, using patches to approximate 5% of the local chord at the root, 15% at the kink, 15% at $2y/B = 0.844$, and 5% at the tip; (3) 12 mm behind the fuselage nose; and (4) 12 mm behind the nacelle leading edge on the outside and 15 mm behind the nacelle leading edge on the inside.

The WBNP configuration is shown in Fig. 1. The shaded areas at the front of the nose, wing, and nacelle show the regions where turbulence production was turned off. This figure also shows the span locations on the wing where pressure taps were located (same for WB). The approximate pressure tap locations on the nacelle are shown in Fig. 2.

A summary of the grid sizes employed is given in Table 4. These grids were made available to the DPW-II committee for use by the participants of the workshop. All grids had a farfield extent of at least 40–50 MAC from the body, where MAC represents the mean aerodynamic chord. Minimum normal spacing at walls was set so that $y^+ \approx 1$. Unfortunately, the 1-to-1 grids turned out to be inadequate in several important respects. These deficiencies will be described in section 4.2.

Force and moment results for all cases are tabulated in Tables 5, 6, and 7. The half model reference area was 72,700 mm², the mean aerodynamic chord was 141.2 mm, and the projected half span was 585.647 mm. The moment reference point was 504.9 mm behind the fuselage nose (in the x -direction), and at a vertical position of $z = -33.92$ mm relative to the origin of the supplied grids. For fixed C_L cases, the angle-of-attack α was adjusted to achieve a lift coefficient of $C_L = 0.5 \pm 0.001$.

It should be noted that because the overset grids in this study had overlapped regions on the body, it was necessary to take into account the overlap-

ping when computing forces and moments, to avoid “double-counting.” The same tool, **overint**,¹⁹ was used to process both OVERFLOW and CFL3D over-set solutions.

For the majority of the cases, the L-2 norm of density-equation residual typically dropped 3–4 orders of magnitude, lift converged to within 0.001, and drag converged to within 0.0001 (=1 drag count). These were considered to be criteria for convergence. Notes are also included in Tables 5–7 to indicate the approximate range in force and moment coefficients for cases that did *not* converge, (i.e., for which the computed forces and moments were oscillatory). In these non-converging cases, the numbers reported in columns 3–7 represent the computed values when the computation was stopped. All runs were performed with local time stepping (not time-accurately).

4 Results

All cases were computed at $M = 0.75$, at a Reynolds number of $Re = 21246.5$ per mm, which corresponds to $Re = 3 \times 10^6$ based on MAC. The grids each represented half of the full configuration, and symmetry boundary conditions were applied along the center plane.

4.1 Comparisons with Experiment

Figs. 3, 4, and 5 show summary plots of CFD compared to experiment. In these plots, all the CFD results used specified transition and the medium (m) sized grids, and all are lumped together without distinguishing between grid types, codes, or turbulence models. These distinctions, as well as the effects of grid density, will be presented in later sections. The case numbers plotted here are 2.1–2.54. The purpose for showing the results in this generic way is to give the reader a feel for (1) the overall variation in the CFD, and (2) how well CFD *on the whole* compared against experiment.

As was also seen for results in the first drag prediction workshop DLR-F4 case, computed lift coefficient for the DLR-F6 was higher than C_L measured experimentally, by between 0.03–0.08 at any given angle of attack. Drag coefficients followed the trend of the experimental results very well, but were somewhat low for WB by about 10–20 drag counts at all lift levels, and were somewhat high for WBNP at the lower lift levels. Moment coefficient values differed from experiment by as much as 0.02–0.03.

Regarding trends, the CFD generally predicted the $\Delta C_L = (C_{L,WBNP} - C_{L,WB})$ of approximately 0.06 between WB and WBNP reasonably well at the higher angles of attack, but predicted too small a

ΔC_L at the lower angles of attack. The ΔC_D was overpredicted by CFD by 20–30 drag counts (30–45%) at the lower lift levels ($C_L < 0.3$); the ΔC_D prediction was better at higher lift levels. Little can be said about the prediction of the moment trends, other than the fact that the difference in slopes between WB and WBNP was generally predicted. The CFD did not capture the breaks in the moment curves near $C_L = 0.55$. At the target condition of $C_L = 0.5$, the ΔC_D in the experiment was 43 counts. CFD predicted ΔC_D between approximately 54 and 59 counts (11–16 counts high compared to experiment).

Typical surface pressure (C_p) comparisons between CFD and experiment are shown at eight span stations for WB in Fig. 6. The CFD results plotted here are case numbers 3.3 and 2.54. Using $C_L = 0.5$ in the CFD resulted in poor comparison with experimental surface pressures. On the other hand, running CFD at the same angle of attack as experiment ($\alpha = 0.49^\circ$) yielded much better comparisons, including correct shock position prediction. The fact that CFD predicted wing pressures in very good agreement with experiment at $\alpha = 0.49^\circ$, yet yielded too high a lift (by over 10%) is difficult to explain. It seems to imply that either (1) the lift force over the fuselage part of the WB configuration was overpredicted by the CFD, or (2) there was a wind tunnel correction or other modeling fidelity issue not being properly accounted for in the CFD runs.

Typical C_p comparisons between CFD and experiment are shown at eight span stations for WBNP in Fig. 7. The CFD results plotted here are case numbers 3.4 and 2.42. Like the WB case, running CFD at the same angle of attack as experiment ($\alpha = 1.0^\circ$) yielded the best results in comparison with experimental pressures; matching the lift yielded worse results. Note the significant disagreement between CFD and experiment at span station $2y/B = 0.331$ on the wing lower surface just inboard of the pylon. This disagreement will be explored in greater detail in section 4.3.1.

4.2 Grid Density Study

Fig. 8 shows the effect of grid density on the WB and WBNP cases, for $C_L = 0.5$ using the SA turbulence model. Experimental levels are included for reference. In these cases, represented by case numbers 1.1–1.6, 1.11–1.15, and 1.17–1.22, the computations were performed fully turbulent. The drag coefficient is plotted as a function of total number of grid points raised to the $-2/3$ power. If the grids are of the same family and lie in the asymptotic region, then a globally-second-order spatially accurate code

(such as CFL3D and OVERFLOW) should produce values that lie in a straight line. Clearly, this is not the case here.

This figure shows some unexpected trends. First, for the WB case using the same overset grids, CFL3D and OVERFLOW appeared to be converging toward *different* solutions as the grid was refined (the curves cross). Considered individually, and making the assumption that the two finest grids lie within the asymptotic region, CFL3D was heading toward an infinitely-refined solution near $C_D = 0.0282$, whereas OVERFLOW was heading toward a value about 10 drag counts lower. This difference indicates that either the two codes had modeled terms or boundary conditions that were not identical, and/or the medium grid (nearly 7 million grid points!) was still not fine enough to lie in the asymptotic region for grid convergence for this case. CFL3D was not able to complete WBNP(f) on the overset grid due to resource limitations, so no firm conclusions can be drawn regarding that case.

The second unexpected trend was the behavior of the WBNP case with CFL3D on the 1-to-1 grids. A relatively large drop in C_D occurred between the medium and fine levels, which appeared to be too large in comparison with the other cases. This discrepancy may in part be a result of several deficiencies in the 1-to-1 grids. The WBNP grid system was generally non-smooth, was non-orthogonal in places (even near the body where normal spacing is generally very desirable), and there were many sudden grid spacing changes when passing from one zone to another. Fig. 9 shows a grid plane around the wing from the WBNP(m) grid, where some of these deficiencies in the 1-to-1 WBNP grid system are evident. (See Rumsey et al.¹⁶ for a list of “best practices”, including grid generation, for aircraft configurations of this type.) Also, for both WB and WBNP, the three levels of grid (c), (m), and (f) were not refined in a consistent fashion. For example, although there were more overall grid points, many parts of the finer grids contained regions where certain directions were not refined at all, or were refined inconsistently. As a result, successive grid levels did not belong to the same grid “families,” and hence cannot exhibit expected convergence characteristics.

In spite of the problems discussed above, this study can give a feeling for the variation in drag coefficient due to changes in grid size. For the WB case, between the medium and fine level grids, the drag changed by 1.1% (3 drag counts) for CFL3D (1-to-1), 0.4% (1 count) for CFL3D (overset), and 3.6% (10 counts) for OVERFLOW (overset). For the WBNP case, between the medium and fine level grids, the

drag changed by 2.7% (9 counts) for CFL3D (1-to-1), and 1.2% (4 counts) for OVERFLOW (overset). Looking at the data another way, if we *estimate* (based on trends in Fig. 8) the infinitely-refined WB solution to be $C_D = 0.0278$, then the maximum error in drag on a fine grid (23 million points) was 1.3% (4 counts), the maximum error on a medium grid (6–7 million points) was 3.7% (10 counts), and the maximum error on a coarse grid (2–4 million points) was 8.2% (23 counts). Similarly, if we *estimate* the infinitely-refined WBNP solution to be $C_D = 0.0334$, then the maximum error in drag on a fine grid (36 million points) was 1.1% (4 counts), the maximum error on a medium grid (9–11 million points) was 2.7% (9 counts) and the maximum error on a coarse grid (3–5 million points) was 7.9% (26 counts).

The picture is less clear when considering grid convergence of the parameter “angle-of-attack needed to achieve $C_L = 0.5$,” shown in Fig. 10. In both WB and WBNP cases, there was no clear trend toward a grid-converged value as the grid was refined.

Fig. 11 shows the effect of grid density on surface pressure coefficient for WB at the two span stations where the biggest differences are visible. This figure plots OVERFLOW results on the overset grids (case numbers 1.17–1.19). CFL3D results, not shown, show similar variation between the three grid levels on the overset grids. At $2y/B = 0.15$, there were significant differences between all three results near the upper surface trailing edge. This is the region where there was a wing-root separation bubble, which will be discussed in greater depth in sections 4.3.2 and 4.3.5. At $2y/B = 0.847$, there was little variation between the coarse and medium grid levels, but a larger change between the medium and fine levels. The biggest change was the shock location, which was probably a result of the lower angle of attack required to match $C_L = 0.5$ on the fine grid. This result highlights the fact that even the medium grid (6.86 million grid points) was not fine enough to capture some key physical features, and thus it is unlikely that its results lie in the asymptotic range of grid convergence. Whether the fine grid (23.15 million grid points) was fine enough cannot be proven without using one or more finer grids. The effects of grid density on surface pressures for WBNP were very similar to those shown for WB, so results are not shown here.

4.3 CFD Variation

4.3.1 Effect of Grid

Section 4.2 described the grid density studies for WB and WBNP. Here we look in detail at one of the

primary differences between results using the 1-to-1 grid system as opposed to the overset grid system in the WBNP case. This difference is believed to be a result of insufficient grid resolution in the 1-to-1 grids used for this study.

Recall Fig. 7, which showed a large difference between CFD and experiment on the wing lower surface at span station $2y/B = 0.331$, just inboard of the pylon. Fig. 12 shows results at this span station using CFL3D on the 1-to-1 grid, CFL3D on the overset grid, and OVERFLOW on the overset grid (case numbers 1.5, 1.15, and 1.21). CFL3D on the 1-to-1 grid predicted a completely different character from either code on the overset grid, yielding surface pressures in good agreement with experiment. Surface pressures are shown in Fig. 13 on the nacelle itself. Results were overall in good agreement with experiment, and each of the three CFD results agreed well with each other, with one exception: the result using the 1-to-1 grid exhibited different behavior on the inboard side ($\Phi = 300^\circ$) from $0.6 < x/c < 1$.

Surface streamlines under the wing near the inboard side of the pylon are shown in Fig. 14 (case number 1.15) and Fig. 15 (case number 1.5) for CFL3D on the overset and 1-to-1 grids, respectively. The overset grid showed a significant region of separation, whereas the 1-to-1 grid showed no sign of separation. Which was the better solution? Grid convergence studies for each grid system, not shown, indicated little effect in this region as each grid was refined. However, the 1-to-1 system was described earlier as having been refined inconsistently, so its grid refinement study was not meaningful. Compared with experiment, the 1-to-1 result was in better agreement, but this may have been coincidence.

A view of the medium overset grid at the inner pylon region is shown in Fig. 16, and the medium 1-to-1 grid is shown in Fig. 17. The overset grid was significantly finer, particularly on and near the pylon. In fact, even the *coarse* overset grid (not shown) was finer than *any* of the 1-to-1 grids in some areas. Based on our experience, and considering the fact that the overset grids utilized uniform grid refinement in all coordinate directions, it is believed that the overset grids were providing the more accurate solution from the numerical point of view. The fact that overset grid results agreed poorly with experiment inboard of the pylon was likely a modeling issue (turbulence model, transition effect, or geometric fidelity).

4.3.2 Effect of Turbulence Model

The effect of three different turbulence models (SA, SST, and EASM-ko) at $C_L = 0.5$, fully turbulent, was assessed for both WB and WBNP us-

ing medium level 1-to-1 grids in CFL3D (case numbers 1.2, 1.5, 1.7–1.10). The results for WB varied from a low of $C_D = 0.02812$ for SST to a high of $C_D = 0.02884$ for SA (7 drag count difference). EASM-ko was between. Most of the drag difference was from the viscous drag component. The three turbulence models differed by less than 1 count in pressure drag. The results for WBNP varied from a low of $C_D = 0.03276$ for SST to a high of $C_D = 0.03430$ for SA (15 drag count difference). Again, most of the drag difference was from the viscous drag component. The three turbulence models differed by less than 6 counts in pressure drag.

OVERFLOW was also used at $C_L = 0.5$, fully turbulent to determine the variation between SA and SST (case numbers 1.18, 1.21, 1.23, and 1.24). For WB, the variation between drag for SA and SST was 1 drag count. SST yielded higher pressure drag than SA (by 4 counts) and lower viscous drag (by 3 counts). For WBNP, the variation between drag for SA and SST was less than 1 drag count. SST yielded higher pressure drag (by 6 counts) and lower viscous drag (by 5 counts).

To show typical results, pressure coefficients are plotted for WBNP(m) using CFL3D on the 1-to-1 grid in Fig. 18 at two of the span stations that show the greatest variation between turbulence models. These results represent case numbers 1.5, 1.8, and 1.10. The most significant differences occurred at the upper surface trailing edge region near the wing root, in the area of the separation bubble. Fig. 19 shows wing root separation size, for the various turbulence models using CFL3D on the 1-to-1 WB(m) and WBNP(m) grids. The x-axis shows the approximate maximum spanwise bubble width on the wing, and the y-axis shows the approximate streamwise bubble length. Thus, a larger bubble is plotted near the upper right of the plot, and a smaller bubble near the lower left. In general, the SA model predicted the largest bubble and EASM-ko predicted the smallest.

The effect of turbulence model was also investigated with transition specified for the WB case, using the medium level 1-to-1 grid. Drag polar results are shown in Fig. 20. The case numbers plotted here are 2.1–2.15 and 2.51–2.53. As discussed in section 4.1, the WB results tended to be to the left of the experimental drag polar. However, the main point here is the variation due to turbulence model. As shown, this variation ranged from 7 drag counts at the lower angles of attack to 14 drag counts at the higher angles. Most of this variation was due to the SST model, which tended to give lower drag levels than the other models in CFL3D. Between SA

and EASM-ko the variation was at most only 2 drag counts over the entire polar range.

4.3.3 Effect of Transition

Several cases were run to determine the effect of fixing transition (at the locations described in section 3), as opposed to running fully turbulent. Note, however, that “fully turbulent” does *not* mean turbulent everywhere. This is a popular misconception. What it really means is that turbulence was *allowed* to develop everywhere, but each model transitioned to turbulence on its own. Precise locations were not determined for the current study. However, Rumsey and Biedron⁵ documented transition locations for CFL3D runs of the the DLR-F4. In that study, SA was found to transition the furthest forward, near 1.4% of the local chord at a particular span station, while EASM-ko was found to transition the furthest aft, near 5.7%. The effect of this transition location difference for a given turbulence model was found to be very small.

Fig. 21 shows a typical effect of transition on surface pressure coefficients, in this case for WBNP(m) using OVERFLOW (case numbers 1.21 and 3.6). Two representative span stations are shown. The differences were very small. Transition did not have much of an effect on the separated region inboard of the pylon, and at $2y/B = 0.411$ the shock position shifted only slightly. For OVERFLOW, transition specified gave a lower drag than fully turbulent by 10 counts for WB, and 5–6 counts for WBNP. For CFL3D, transition specified gave a lower drag than fully turbulent by 10 counts for WB (1-to-1) and by 7 counts for WB (overset); transition specified gave a lower drag than fully turbulent by 11 counts for WBNP (1-to-1), but it gave a *higher* drag by 4 counts for WBNP (overset). The reason for this discrepancy (WBNP transition specified giving higher drag than fully turbulent using CFL3D) may be related to the inboard pylon separation.

4.3.4 Effect of Code

Figs. 22, 23, and 24 show differences in forces and moments predicted by CFL3D and OVERFLOW for both the WB and WBNP cases, on the overset medium grid using SA with transition specified. These plots represent case numbers 2.16–2.54, 2.23–2.29, 2.37–2.43, and 2.44–2.50. CFL3D yielded lower lift values at a given angle of attack than OVERFLOW for all cases. The maximum difference in lift coefficient was 0.0362 for WBNP at $\alpha = -1.5$, the maximum difference in drag coefficient was 0.00151 for WB at $\alpha = 1.5$, and the maximum difference in moment coefficient was 0.0132 for WBNP at $\alpha = 1.5$.

Typical pressure coefficients for CFL3D and OVERFLOW are plotted for WB in Fig. 25, for $C_L = 0.5$ fully turbulent (case numbers 1.12 and 1.23). The two span stations shown exhibited the largest differences between the two codes. The sensitive wing-root-juncture separated region was predicted differently by the two codes, and also at $2y/B = 0.847$ OVERFLOW predicted the shock to be slightly forward of the shock predicted by CFL3D.

4.3.5 Effect of Viscous Model

CFL3D was run with SA fully turbulent on the WB(m) overset case with $C_L = 0.5$, both in the code’s “typical” operational mode of thin layer in the body-normal direction (t1), as well as with thin layer in all three directions (t3). These were case numbers 1.12 and 1.27. To achieve $C_L = 0.5$, the t1 case required $\alpha = 0.190^\circ$, whereas t3 required $\alpha = 0.113^\circ$. The resulting drag coefficients were different by only 1.4 counts, with t3 higher. Although not shown, surface pressure coefficients were very similar between the two cases.

At a fixed angle of attack of $\alpha = 0.49^\circ$, with SA transition specified, CFL3D was again run on the overset WB(m) grid in t1 and t3 modes (case numbers 2.54 and 2.55). Here, the resulting t3 lift coefficient was higher than that for t1 by 0.0114, and the t3 drag coefficient was higher than that for t1 by 5.3 counts. Surface pressure coefficients at two span stations are shown in Fig. 26. There are only small differences visible in the figure.

OVERFLOW was used to determine the differences between t1 and full Navier-Stokes for both the WB(m) and WBNP(m) cases at $C_L = 0.5$, using SA fully turbulent. For WB(m) (case numbers 1.18 and 1.25), the angle of attack was $\alpha = 0.1162^\circ$ for t1 and 0.202° for full. The drag coefficient for full was higher than that for t1 by 3.6 counts. For WBNP(m) (case numbers 1.21 and 1.26), the angle of attack was 0.6863 for t1 and 0.830 for full. The drag coefficient for full was higher than that for t1 by 4.8 counts. The biggest noticeable change between t1 and full in the flowfields occurred in the wing-root-juncture region of separated flow. Plots showing the upper surface streamlines and bounding isosurface of reverse flow for WBNP using t1 and full are shown in Figs. 27 and 28, respectively. The full solution yielded a significantly larger bubble than the t1 solution. The reverse flow region inboard of the pylon (not shown) was not affected as much. Although not shown, for WB the full solution also yielded a larger wing-root separation bubble than the t1 solution, but the difference was not as pronounced as for WBNP.

OVERFLOW was also used to evaluate the effect of t1 vs. full for WB(m) with the SST turbulence model (case numbers 1.23 and 1.28). The angle of attack was $\alpha = 0.3075^\circ$ for t1 and 0.3518° for full. The drag coefficient for full was nearly the same as that for t1 (only 0.8 drag counts higher). It is interesting to note the effect of t1 vs. full on the angle of attack necessary to achieve $C_L = 0.5$. This effect is shown using OVERFLOW on the overset WB(m) grid for both SA and SST in Fig. 29. The dashed line shows part of the SA (transition specified) C_L - α curve, given earlier in Fig. 22, and the square symbols represent the experimental data. Computing with fully turbulent as opposed to transition specified shifted the result somewhat to the right, and using full as opposed to t1 shifted the result to the right even further. Furthermore, both SST results were to the right of the SA results. This figure indicates that *part* of the reason for lift overprediction may be due to choice of turbulence model and viscous model. However, comparisons should be made between experiment and transition-specified computations. In this context, the lift would still be overpredicted by as much as $C_L = 0.03$ using SST and full Navier-Stokes. Surface pressure coefficients at two representative span stations in Fig. 30 show only relatively small effects between the four cases. The biggest change in shock position at $2y/B = 0.411$ was due to SST (further aft) vs. SA (further forward); t1 vs. full had very little effect.

5 Summary and Conclusions

In summary, the two CFD codes OVERFLOW and CFL3D were used to quantify CFD variations for a wing-body (WB) and wing-body-nacelle-pylon (WBNP) DLR-F6 configuration used in the second drag prediction workshop (DPW-II) sponsored by AIAA. Comparisons were also made with experiment. In general, lift was overpredicted for both WB and WBNP, and drag was underpredicted for WB and overpredicted (at low angles) for WBNP. The reason for lift overprediction, which almost all CFD methods presented at the DPW-II workshop had in common, is not known. Trends in ΔC_D were overpredicted by 20–30 drag counts (30–45%) at lower lift levels ($C_L < 0.3$). At the target condition of $C_L = 0.5$, ΔC_D was overpredicted by between 11–16 counts. This study demonstrated that performing the CFD calculation at the same angle-of-attack as experiment resulted in good comparisons with wing surface pressures, but matching lift ($C_L = 0.5$) did not.

Grid density studies performed at the $C_L = 0.5$ condition were not definitive. The 1-to-1 grids were

of poor quality and inconsistently refined, so no firm conclusions were possible. The overset grids were of higher quality, but produced inconsistent trends between the two codes, indicating the likelihood that the medium level grids of 6–11 million points still were not fine enough to produce results that lie in the asymptotic range for second-order grid convergence for these cases. However, by estimating trends, it appears that the medium level grids were in error by roughly 10 drag counts from an infinitely refined grid.

Detailed studies of CFD variation due to mesh type, turbulence model, transition, code, and viscous model were performed. Many results were discussed. Here, some key points are summarized:

- A particular effect of grid was noted inboard of the pylon for WBNP; using the SA turbulence model, the poorer quality, less resolved 1-to-1 grids yielded no separation, whereas the overset grids predicted large separation. The 1-to-1 results were in better agreement with experiment, but for the wrong reasons.
- In CFL3D, turbulence models had effects on the wing-root separation bubble size; SA predicted the largest bubble, EASM-ko the smallest.
- In CFL3D, the SST turbulence model consistently predicted lower drag than SA and EASM-ko. Across the drag polar, variation in C_D was 7–14 counts. In OVERFLOW, there was less of a difference between SA and SST drag levels.
- With one exception, using “transition specified” gave lower C_D than “fully turbulent” by 5–11 counts.
- Within the range tested, at a fixed angle of attack CFL3D yielded consistently lower C_L than OVERFLOW by as much as 0.036; drag was at most 15 counts different, and moment coefficient was at most 0.0132 different.
- The viscous model (thin vs. full Navier-Stokes) had its most noticeable effect on the wing-root separated region; full Navier-Stokes predicted a larger bubble. The effect on drag was at most 5 drag counts. The maximum effect of t3 vs. t1 was similar.

As a final summary plot, Fig. 31 shows the maximum variation in drag count due to each of five categories evaluated at $C_L = 0.5$ (Case I). Note that all of these results arise from computations on medium level grids (approximately 6–7 million grid points for WB and 8–11 million grid points for WBNP).

As mentioned above, the medium level grids were possibly as much as 10 drag counts in error from an infinitely refined grid.

If all of these variations were additive, then the total variation due to the CFD sources of grid type, code, turbulence model, transition, and viscous model could be as much as 52 drag counts (for WBNP) on a medium-level grid! Realistically, of course, the effects would not all be additive. Also, the effect of transition probably should not be counted, because if the CFD codes were run all fully turbulent or all fixed transition, then variations due to this parameter would be very small. Nonetheless, from this study it is easy to see why the drag prediction workshops have shown variations among participants of as much as 25–50 drag counts.

Clearly, some variation in CFD results should always be expected. In order to meet the application's needs, the challenge is to understand and quantify this variation, and then use it to gain confidence in the predictions. This task is difficult to accomplish on complex cases; future workshops using simpler "unit problems" could help to better isolate individual causes. Assessment of variation will be particularly important as we begin to tackle increasingly complex flows outside of normal cruise conditions, including flows with larger regions of separation.

References

1. Redeker, G., "DLR-F4 Wing Body Configuration," AGARD-AR-303, *A Selection of Experimental Test Cases for the Validation of CFD Codes*, Vol. 2, August 1994, pp. B4-1 – B4-21.
2. Levy, D. W., Zickuhr, T., Vassberg, J., Agrawal, S., Wahls, R. A., Pirzadeh, S., and Hemsch, M. J., "Data Summary from the First AIAA Computational Fluid Dynamics Drag Prediction Workshop," *Journal of Aircraft*, Vol. 40, No. 5, 2003, pp. 875–882; also AIAA Paper 2002-0841, January 2002.
3. Hemsch, M., "Statistical Analysis of CFD Solutions from the Drag Prediction Workshop," AIAA Paper 2002-0842, January 2002.
4. Vassberg, J. C., Buning, P. G., and Rumsey, C. L., "Drag Prediction for the DLR-F4 Wing/Body using OVERFLOW and CFL3D on an Overset Mesh," AIAA Paper 2002-0840, January 2002.
5. Rumsey, C. L. and Biedron, R. T., "Computation of Flow Over a Drag Prediction Workshop Wing/Body Transport Configuration Using CFL3D," NASA/TM-2001-211262, December 2001.
6. Brodersen, O. and Sturmer, A., "Drag Prediction of Engine-Airframe Interference Effects Using Unstructured Navier-Stokes Calculations," AIAA Paper 2001-2414, June 2001.
7. Slotnick, J. P., Kandula, M., and Buning, P. G., "Navier-Stokes Simulation of the Space Shuttle Launch Vehicle Flight Transonic Flowfield Using a Large Scale Chimera Grid System," AIAA Paper 94-1860, June 1994.
8. Palmer, G., Buning, P. G., Yanowitz, H., and Venkatapathy, E., "Three-Dimensional Computational Analysis of Complex Launch Vehicle Configurations," *Journal of Spacecraft and Rockets*, Vol. 33, No. 1, Jan.-Feb. 1996, pp. 49–53.
9. Slotnick, J. P., An, M. Y., Mysko, S. J., and Yeh, D. T., "Navier-Stokes Analysis of a High-Wing Transport High-Lift Configuration With Externally Blown Flaps," AIAA Paper 2000-4219, Aug. 2000.
10. Buning, P. G., Wing, T. C., Dilley, A. D., and Pao, J. L., "Prediction of Hyper-X Stage Separation Aerodynamics Using CFD," AIAA Paper 2000-4009, Aug. 2000.
11. Krist, S. L., Biedron, R. T., and Rumsey, C. L., "CFL3D User's Manual (Version 5.0)," NASA TM-1998-208444, June 1998.
12. Spalart, P. R. and Allmaras, S. R., "A One-Equation Turbulence Model for Aerodynamic Flows," *La Recherche Aeronautique*, No. 1, 1994, pp. 5–21.
13. Menter, F. R., "Two-Equation Eddy-Viscosity Turbulence Models for Engineering Applications," *AIAA Journal*, Vol. 32, No. 8, 1994, pp. 1598–1605.
14. Rumsey, C. L. and Gatski, T. B., "Recent Turbulence Model Advances Applied to Multielement Airfoil Computations," *Journal of Aircraft*, Vol. 38, No. 5, 2001, pp. 904–910.
15. Rumsey, C. L. and Gatski, T. B., "Summary of EASM Turbulence Models in CFL3D with Validation Test Cases," NASA/TM-2003-212431, June 2003.
16. Rumsey, C. L., Allison, D. O., Biedron, R. T., Buning, P. G., Gainer, T. G., Morrison, J. H.,

Rivers, S. M., Mysko, S. J., and Witkowski, D. P., “CFD Sensitivity Analysis of a Modern Civil Transport Near Buffet-Onset Conditions,” NASA/TM-2001-211263, December 2001.

17. Gatski, T. B. and Speziale, C. G., “On Explicit Algebraic Stress Models for Complex Turbulent Flows,” *Journal of Fluid Mechanics*, Vol. 254, 1993, pp. 59–78.
18. Jongen, T. and Gatski, T. B., “General Explicit Algebraic Stress Relations and Best Approximation for Three-Dimensional Flows,” *Int. J. of Engineering Science*, Vol. 36, 1998, pp. 739–763.
19. Chan, W. M. and Buning, P. G., “User’s Manual for FOMOCO Utilities - Force and Moment Computation Tools for Overset Grids,” NASA TM-110408, July 1996.

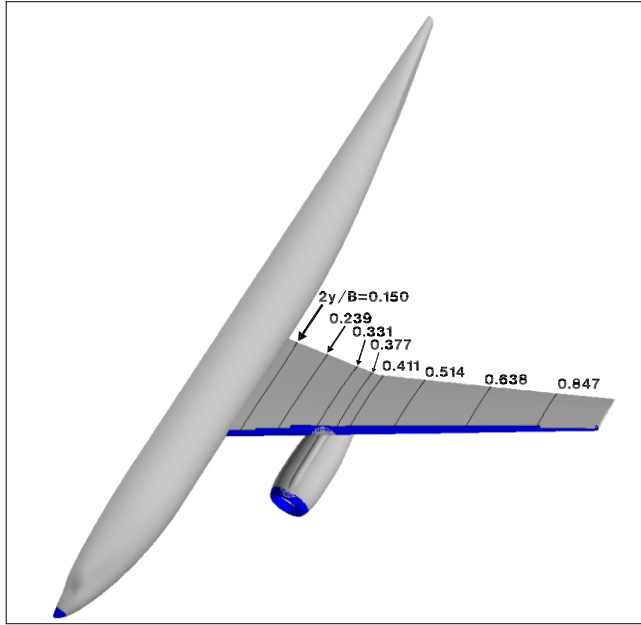


Figure 1. WBNP configuration, showing “transition-specified” regions (shaded) and locations of wing pressure taps.

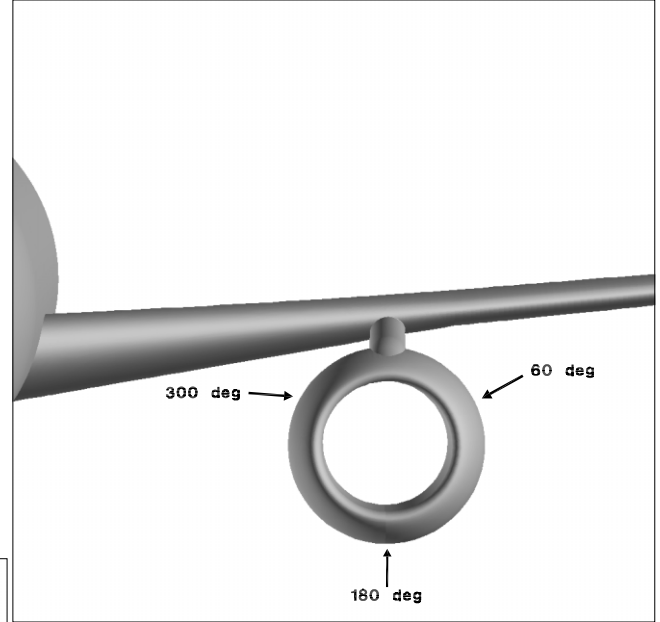


Figure 2. Locations of pressure taps on the nacelle.

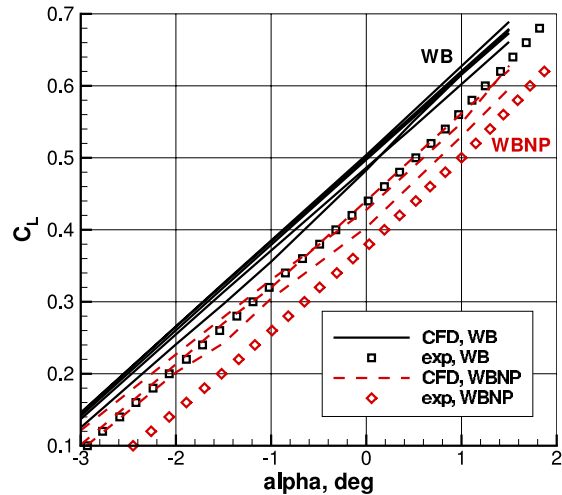


Figure 3. Summary plot of CFD (transition specified) compared to experiment, C_L vs. angle of attack.

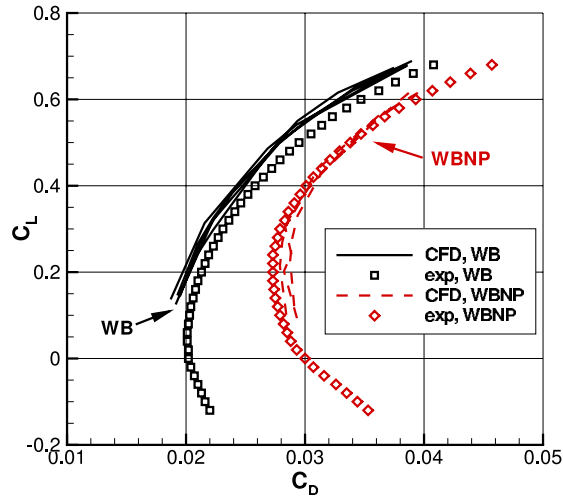


Figure 4. Summary plot of CFD (transition specified) compared to experiment, C_L vs. C_D drag polar.

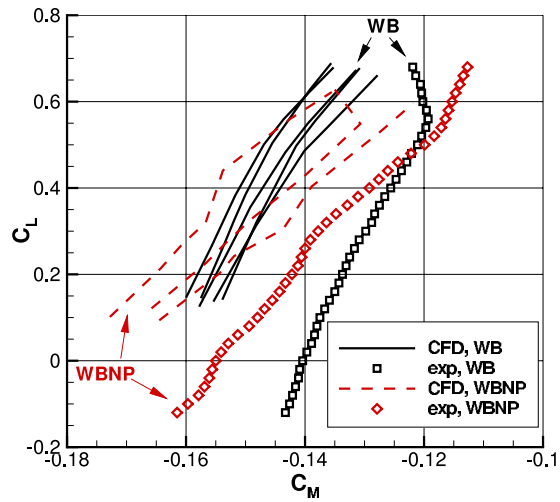


Figure 5. Summary plot of CFD (transition specified) compared to experiment, C_L vs. C_M .

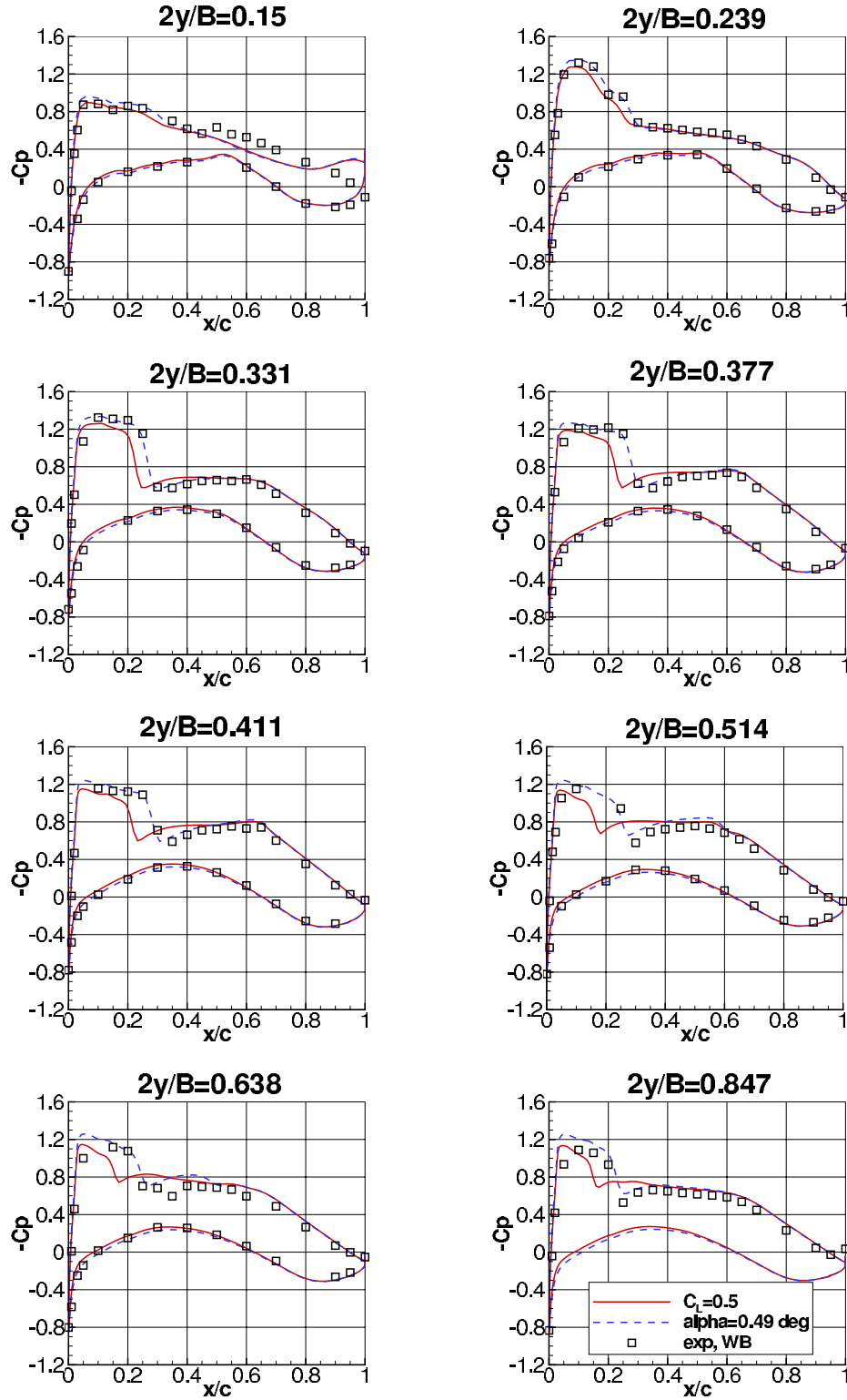


Figure 6. Typical surface pressure comparison for WB(m), showing effect of matching lift vs. matching angle-of-attack, CFL3D, overset grid, SA, transition specified.

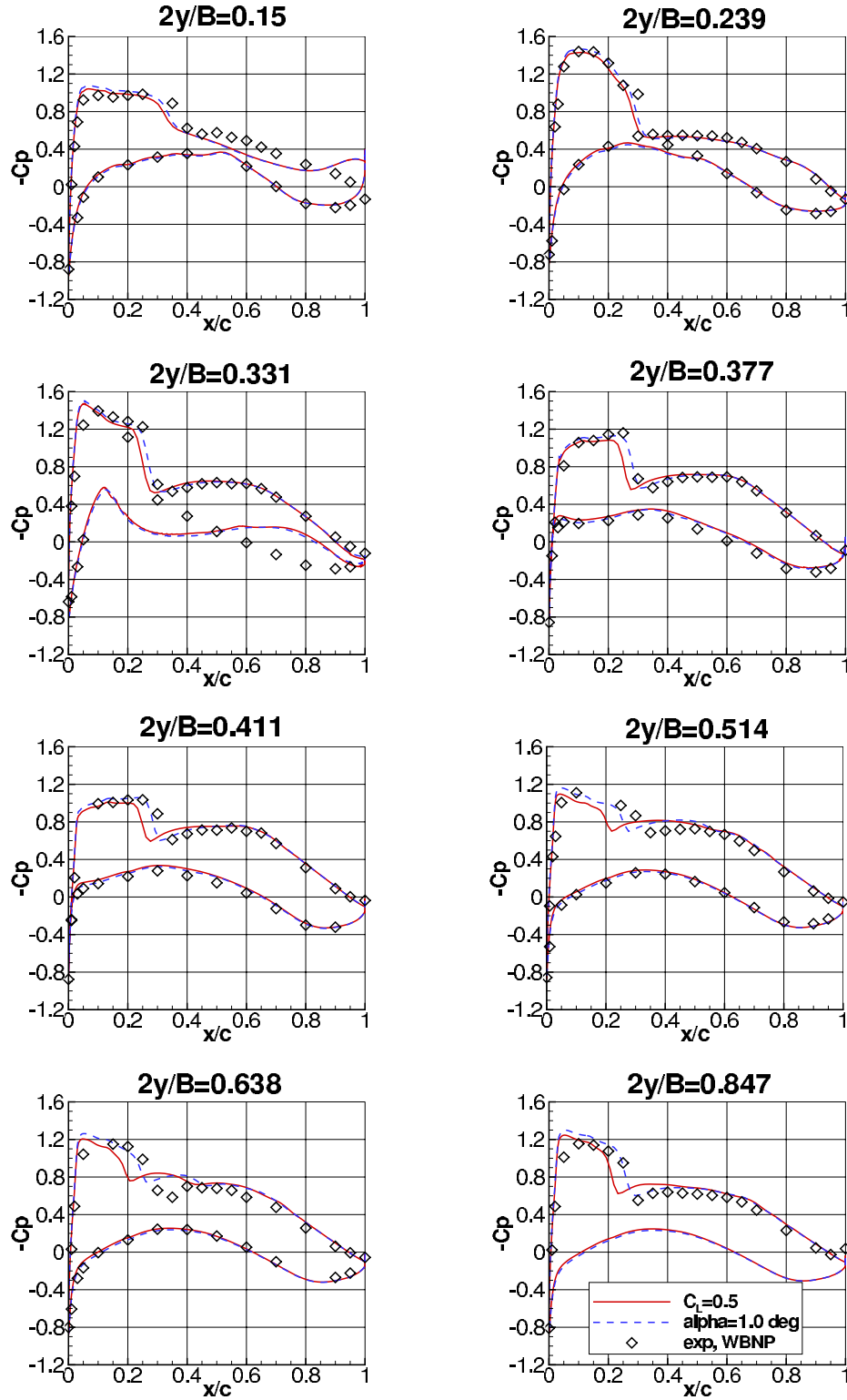


Figure 7. Typical surface pressure comparison for WBNP(m), showing effect of matching lift vs. matching angle-of-attack, CFL3D, overset grid, SA, transition specified.

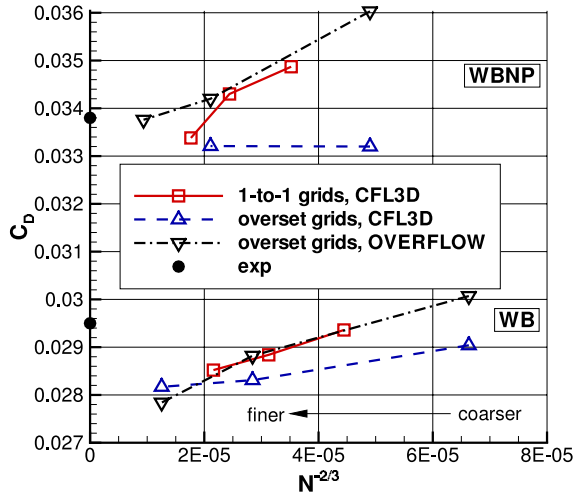


Figure 8. Effect of grid on drag coefficient at $C_L = 0.5$, SA, fully turbulent.

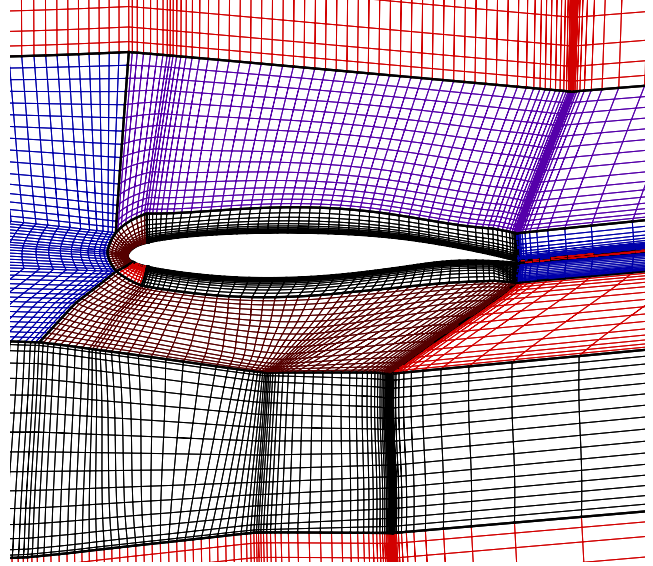


Figure 9. Section of WBNP(m) grid near $2y/B = 0.514$, showing non-smoothness, non-orthogonality, and sudden grid spacing changes.

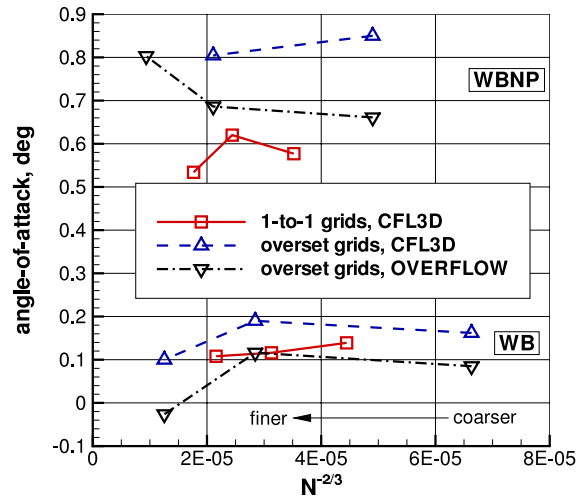


Figure 10. Effect of grid on angle-of-attack needed to achieve $C_L = 0.5$, SA, fully turbulent.

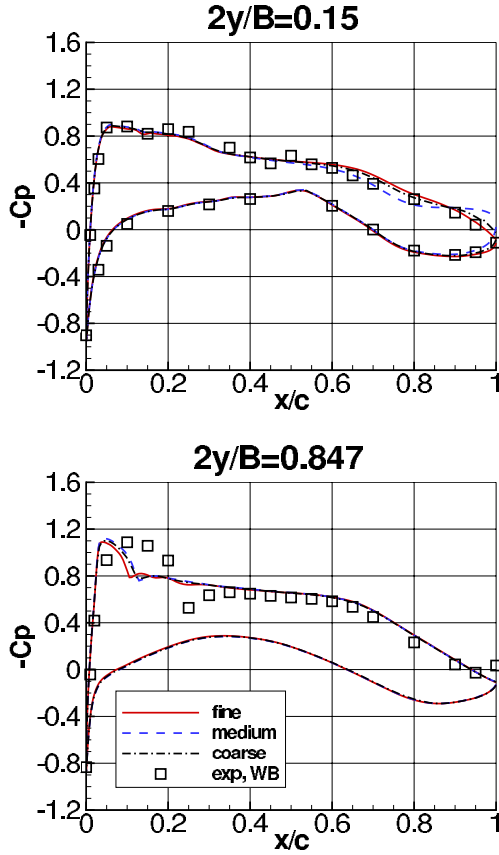


Figure 11. Effect of grid on surface pressure coefficient for WB, $C_L = 0.5$, OVERFLOW, overset grids, SA, fully turbulent.

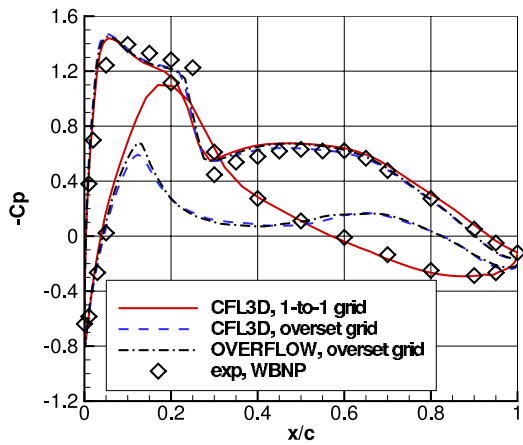


Figure 12. WBNP(m) wing surface pressures at $2y/B = 0.331$, $C_L = 0.5$, SA, fully turbulent.

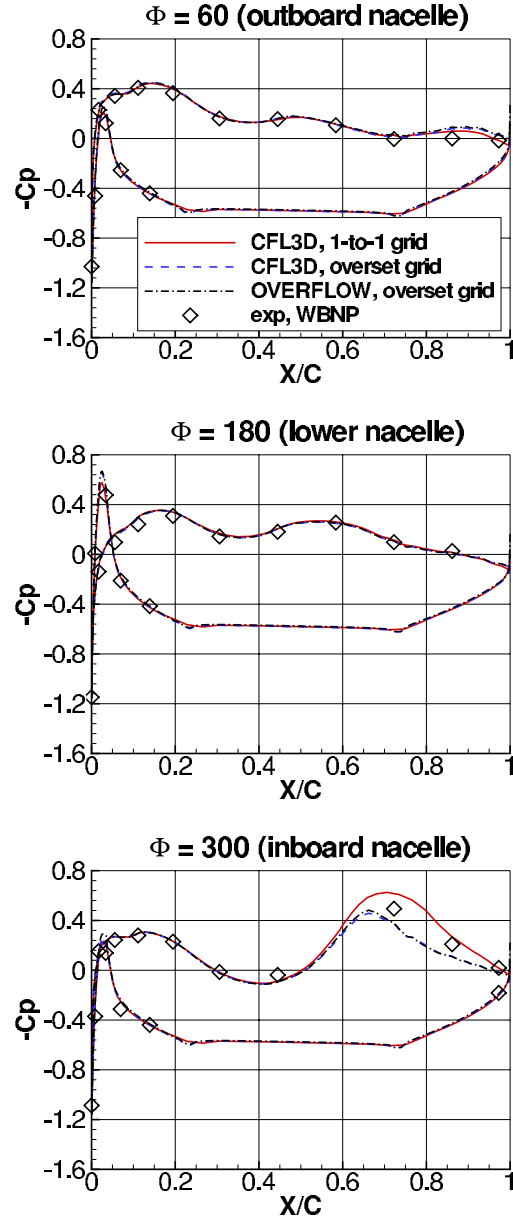


Figure 13. WBNP(m) nacelle surface pressure coefficients $C_L = 0.5$, SA, fully turbulent.

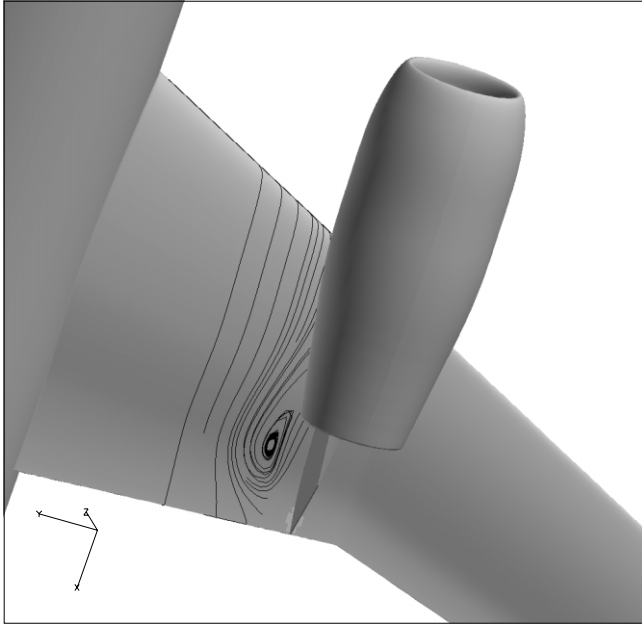


Figure 14. WBNP(m) streamlines on the underside of the wing near the inboard nacelle, CFL3D, overset grid, SA, fully turbulent.

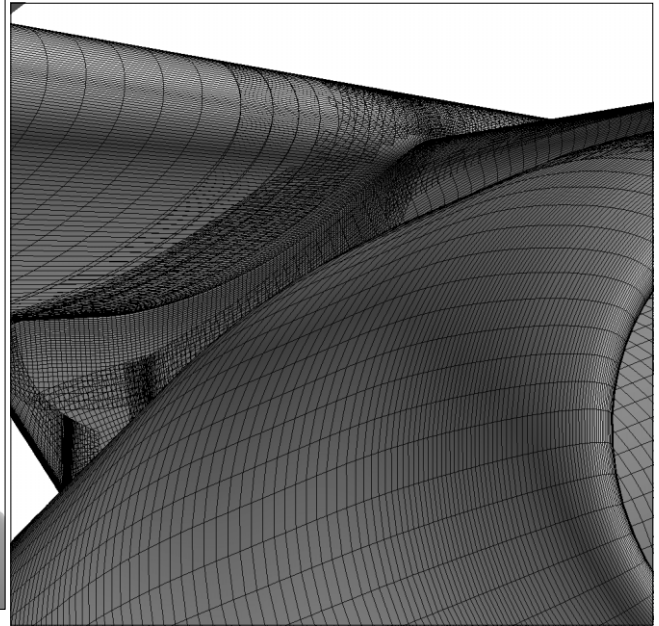


Figure 16. View of overset WBNP(m) surface grid near inboard pylon region.

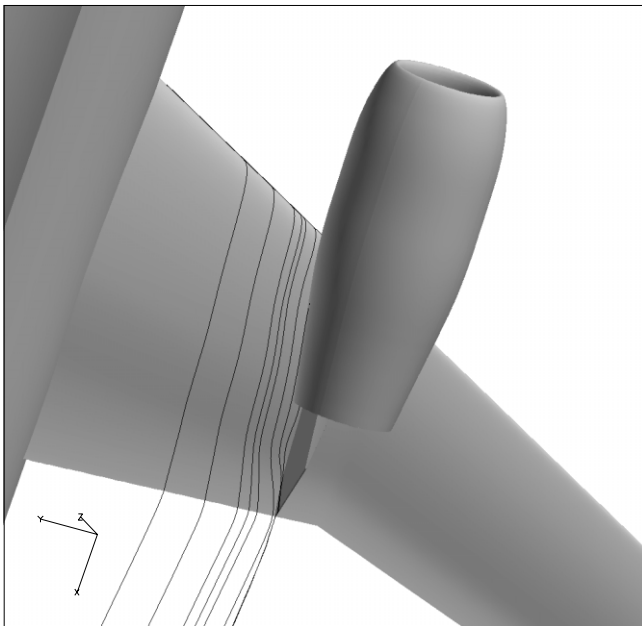


Figure 15. WBNP(m) streamlines on the underside of the wing near the inboard nacelle, CFL3D, 1-to-1 grid, SA, fully turbulent.

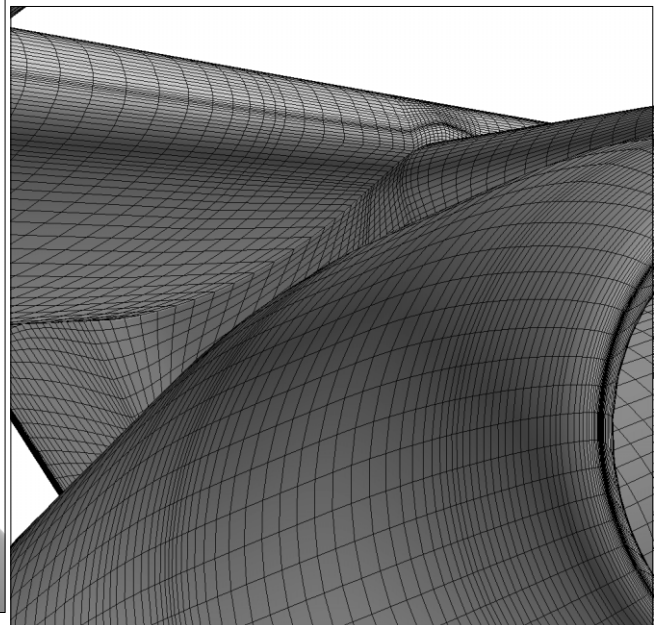


Figure 17. View of 1-to-1 WBNP(m) surface grid near inboard pylon region.

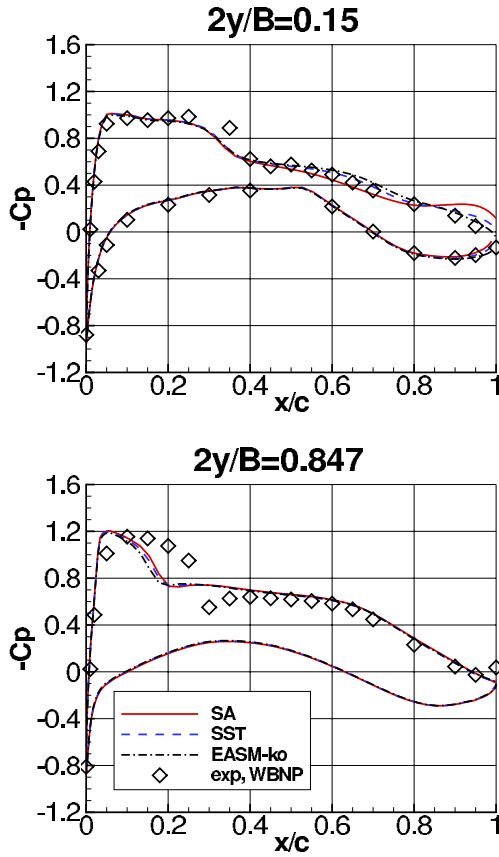


Figure 18. Effect of turbulence model on surface pressure coefficient for WBNP(m), $C_L = 0.5$, CFL3D, 1-to-1 grid, fully turbulent.

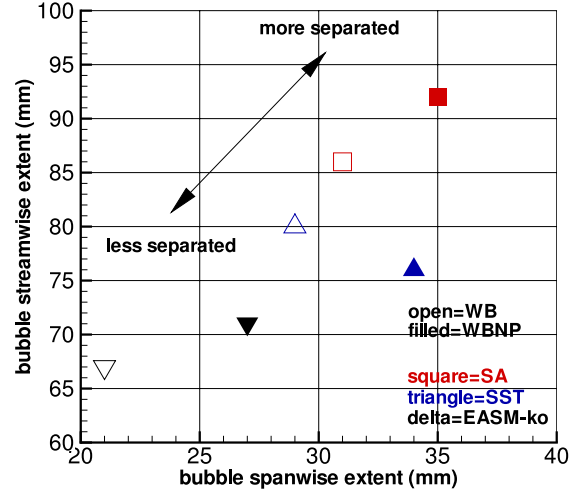


Figure 19. Wing root separation bubble width and length, $C_L = 0.5$, CFL3D on 1-to-1 medium grids, fully turbulent.

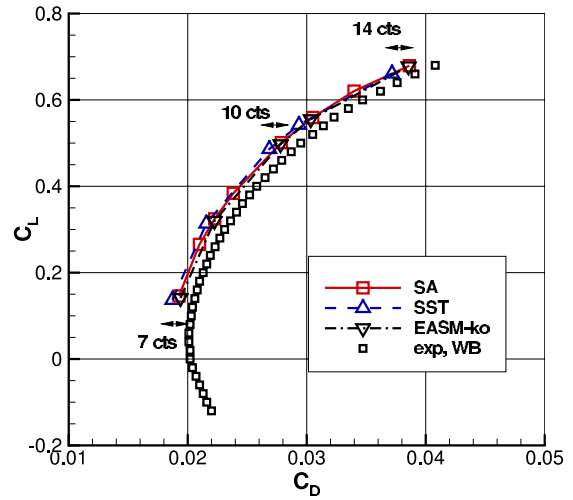


Figure 20. Drag polar showing effect of turbulence model for WB(m), CFL3D, 1-to-1 grid, transition specified.

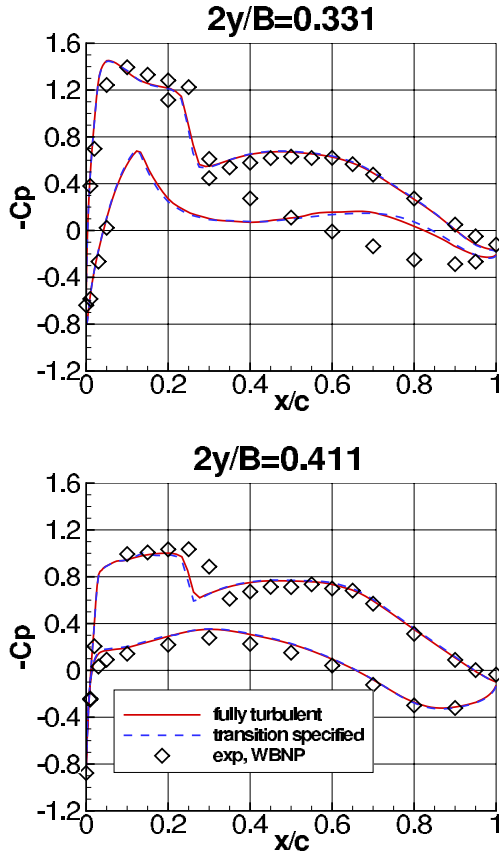


Figure 21. Effect of fully turbulent vs. transition specified on surface pressure coefficient for WBNP(m), $C_L = 0.5$, OVERFLOW, overset grid, SA.

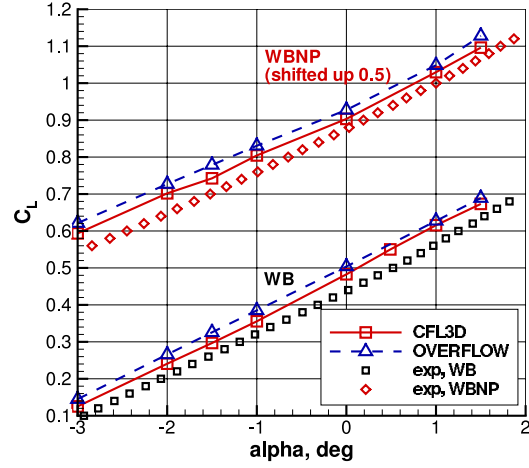


Figure 22. Effect of code, C_L vs. angle of attack, overset medium grids, SA, transition specified (WBNP results shifted up 0.5 for clarity).

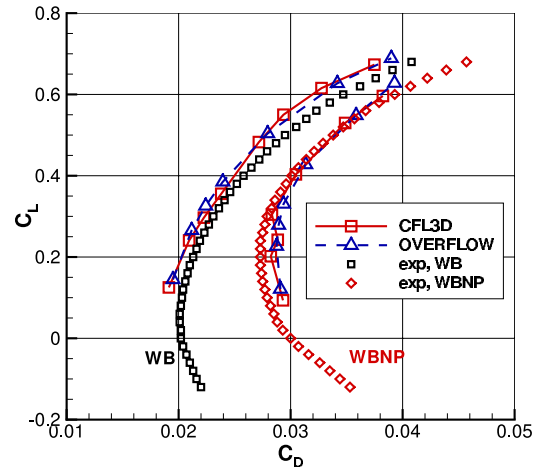


Figure 23. Effect of code, C_L vs. C_D drag polar, overset medium grids, SA, transition specified.

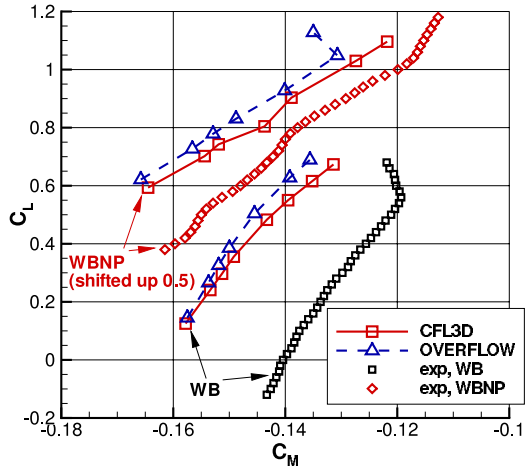


Figure 24. Effect of code, C_L vs. C_M , overset medium grids, SA, transition specified (WBNP results shifted up 0.5 for clarity).

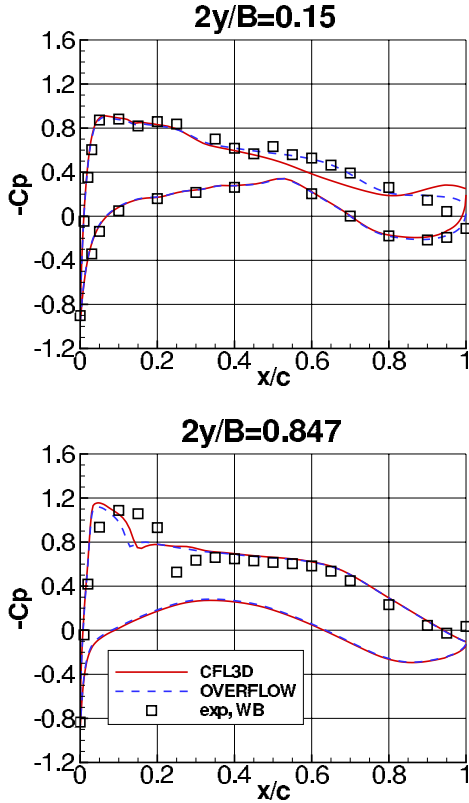


Figure 25. Effect of code on surface pressure coefficient for WB(m), $C_L = 0.5$, overset grid, SA, fully turbulent.

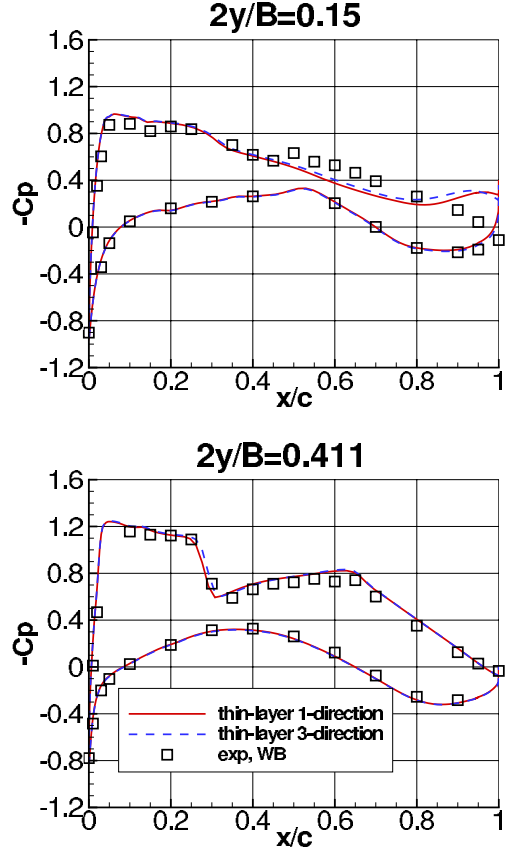


Figure 26. Effect of viscous model (t1 vs. t3) on surface pressure coefficient for WB(m), $\alpha = 0.49^\circ$, CFL3D, overset grid, SA, transition specified.

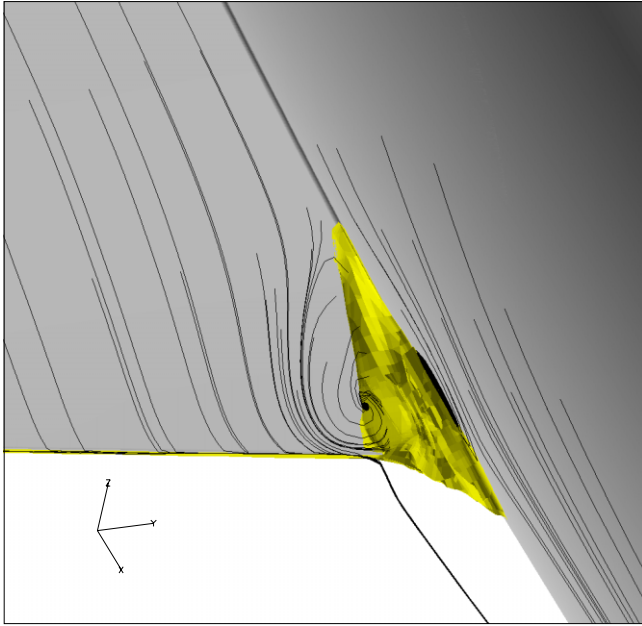


Figure 27. Streamlines and bounding isosurface of reverse flow in the wing-root-juncture region for WBNP(m), $C_L = 0.5$, OVERFLOW, SA, fully turbulent, thin-layer 1-direction (t1).

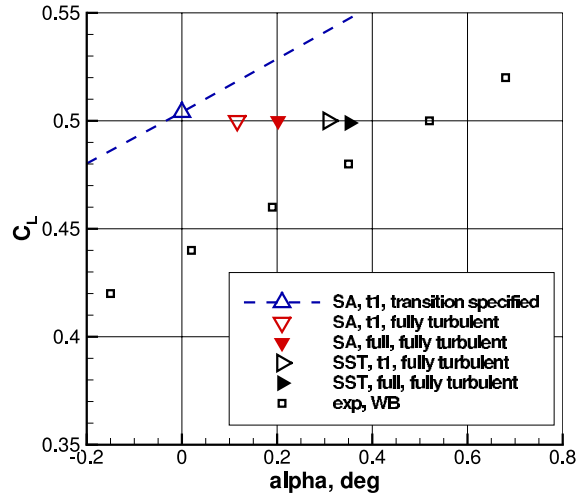


Figure 29. Effect of viscous model using SA and SST for WB(m), C_L vs. angle of attack, overset grid, OVERFLOW.

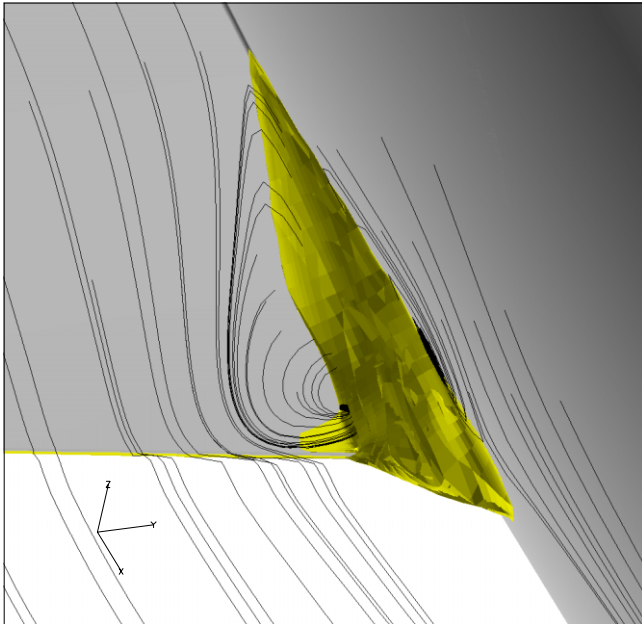


Figure 28. Streamlines and bounding isosurface of reverse flow in the wing-root-juncture region for WBNP(m), $C_L = 0.5$, OVERFLOW, SA, fully turbulent, full N-S.

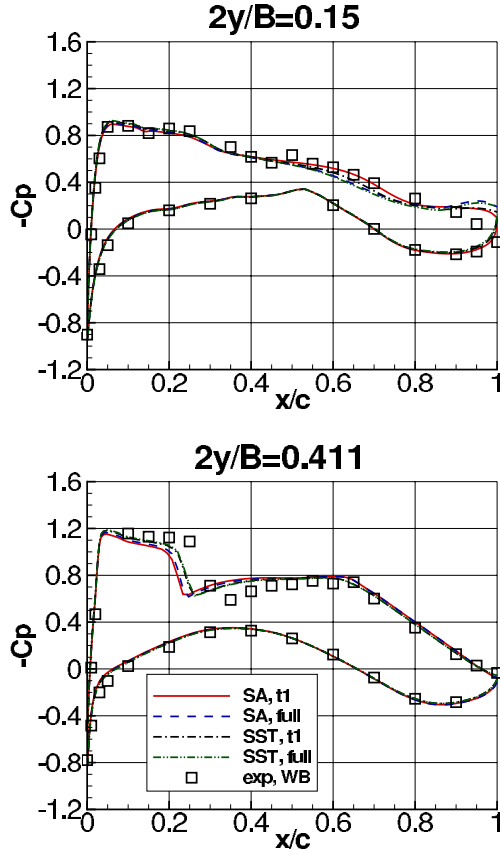


Figure 30. Effect of viscous model on surface pressure coefficient using SA and SST for WB(m), OVERFLOW, $C_L = 0.5$, fully turbulent.

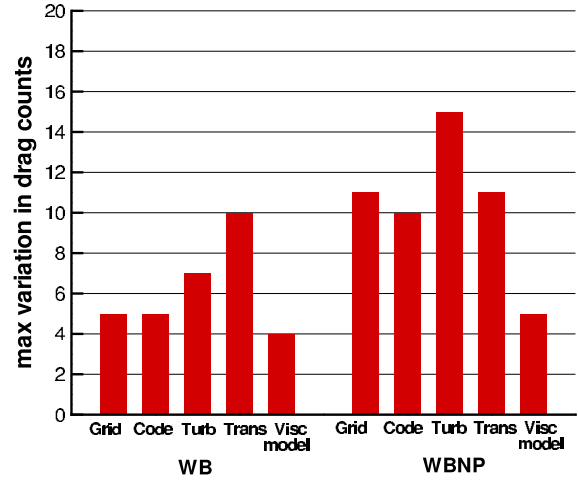


Figure 31. Summary of various effects on drag at $C_L = 0.5$ (Case I), using medium grids.

Table 1. Case Number Designations for Case I - $C_L = 0.5$, “fully turbulent”

Code	Visc. model	Turb. model	WB(c)	WB(m)	WB(f)	WBNP(c)	WBNP(m)	WBNP(f)
C-1to1	t3	SA	1.1	1.2	1.3	1.4	1.5	1.6
C-1to1	t3	SST		1.7			1.8	
C-1to1	t3	EASM-ko		1.9			1.10	
C-overset	t1	SA	1.11	1.12	1.13	1.14	1.15	1.16 (not done)
O-overset	t1	SA	1.17	1.18	1.19	1.20	1.21	1.22
O-overset	t1	SST		1.23			1.24	
O-overset	full	SA		1.25			1.26	
C-overset	t3	SA		1.27				
O-overset	full	SST		1.28				

Table 2. Case Number Designations for Case II - Drag Polar, “transition specified”

Code	Visc. model	Turb. model	Case	-3 deg	-2 deg	-1.5 deg	-1 deg	0 deg	1 deg	1.5 deg	0.49 deg
C-1to1	t3	SA	WB(m)	2.1	2.2	2.3	2.4	2.5	2.6	2.7	2.51
C-1to1	t3	SST	WB(m)	2.8		2.9		2.10		2.11	2.52
C-1to1	t3	EASM-ko	WB(m)	2.12		2.13		2.14		2.15	2.53
C-overset	t1	SA	WB(m)	2.16	2.17	2.18	2.19	2.20	2.21	2.22	2.54
C-overset	t3	SA	WB(m)								2.55
O-overset	t1	SA	WB(m)	2.23	2.24	2.25	2.26	2.27	2.28	2.29	
C-1to1	t3	SA	WBNP(m)	2.30	2.31	2.32	2.33	2.34	2.35	2.36	
C-overset	t1	SA	WBNP(m)	2.37	2.38	2.39	2.40	2.41	2.42	2.43	
O-overset	t1	SA	WBNP(m)	2.44	2.45	2.46	2.47	2.48	2.49	2.50	

Table 3. Case Number Designations for Case III - $C_L = 0.5$, “transition specified”

Code	Visc. model	Turb. model	WB(m)	WBNP(m)
C-1to1	t3	SA	3.1	3.2
C-overset	t1	SA	3.3	3.4
O-overset	t1	SA	3.5	3.6

Table 4. Summary of Grids

Grid	Type	Field nodes (millions)	Field cells (millions)	Zones
WB(c)	1-to-1	3.58	3.37	21
WB(m)	1-to-1	6.04	5.72	27
WB(f)	1-to-1	10.42	9.97	32
WBNP(c)	1-to-1	5.15	4.79	47
WBNP(m)	1-to-1	8.88	8.29	58
WBNP(f)	1-to-1	14.28	13.48	58
WB(c)	overset	1.97	1.85	12
WB(m)	overset	6.86	6.59	12
WB(f)	overset	23.15	22.54	12
WBNP(c)	overset	3.11	2.91	23
WBNP(m)	overset	10.78	10.33	23
WBNP(f)	overset	35.95	34.94	23

Table 5. Force and Moment Results for Case I

Case	α , deg	C_L	C_{M_y}	C_{D_p}	C_{D_v}	$C_{D_{tot}}$	Notes
1.1	0.1390	0.500	-0.1381	0.01602	0.01334	0.02936	
1.2	0.1160	0.500	-0.1406	0.01562	0.01322	0.02884	
1.3	0.1080	0.500	-0.1406	0.01536	0.01316	0.02852	
1.4	0.5770	0.500	-0.1420	0.01873	0.01615	0.03487	
1.5	0.6200	0.500	-0.1413	0.01843	0.01587	0.03430	
1.6	0.5340	0.500	-0.1451	0.01754	0.01583	0.03338	
1.7	0.1700	0.500	-0.1357	0.01555	0.01257	0.02812	
1.8	0.5870	0.500	-0.1413	0.01800	0.01476	0.03276	
1.9	0.1000	0.500	-0.1370	0.01555	0.01306	0.02861	
1.10	0.5140	0.500	-0.1434	0.01786	0.01539	0.03325	
1.11	0.1620	0.500	-0.1380	0.01503	0.01402	0.02904	
1.12	0.1900	0.500	-0.1380	0.01504	0.01327	0.02831	
1.13	0.1000	0.501	-0.1412	0.01492	0.01325	0.02817	dcl=.010,dcd=.0004,dcm=.002
1.14	0.8500	0.501	-0.1183	0.01687	0.01635	0.03320	dcl=.003,dcd=.0003,dcm=.002
1.15	0.8045	0.499	-0.1256	0.01751	0.01570	0.03321	dcl=.001,dcd=.0002,dcm<.001
1.16	-	-	-	-	-	-	not done
1.17	0.0849	0.500	-0.1374	0.01605	0.01402	0.03007	
1.18	0.1162	0.500	-0.1388	0.01537	0.01345	0.02882	
1.19	-0.0263	0.500	-0.1469	0.01438	0.01346	0.02784	dcd=.0001
1.20	0.6610	0.500	-0.1282	0.01944	0.01659	0.03603	dcd<.0001
1.21	0.6863	0.500	-0.1303	0.01816	0.01604	0.03420	
1.22	0.8030	0.499	-0.1275	0.01801	0.01575	0.03376	dcl=.004,dcd=.0003,dcm=.001
1.23	0.3075	0.500	-0.1296	0.01577	0.01315	0.02892	
1.24	0.9206	0.499	-0.1187	0.01873	0.01554	0.03426	
1.25	0.2020	0.500	-0.1342	0.01582	0.01336	0.02918	
1.26	0.8300	0.499	-0.1228	0.01882	0.01585	0.03468	
1.27	0.1130	0.500	-0.1406	0.01516	0.01329	0.02845	
1.28	0.3518	0.499	-0.1261	0.01603	0.01297	0.02900	dcd<.0001

Table 6. Force and Moment Results for Case II

Case	α , deg	C_L	C_{M_y}	C_{Dp}	C_{Dv}	$C_{D_{tot}}$	Notes
2.1	-3.00	0.1461	-0.1600	0.00646	0.01281	0.01927	
2.2	-2.00	0.2654	-0.1557	0.00818	0.01281	0.02099	
2.3	-1.50	0.3246	-0.1537	0.00947	0.01280	0.02227	
2.4	-1.00	0.3836	-0.1517	0.01105	0.01277	0.02383	
2.5	0.00	0.5010	-0.1469	0.01520	0.01267	0.02787	
2.6	1.00	0.6204	-0.1394	0.02150	0.01248	0.03398	
2.7	1.50	0.6792	-0.1352	0.02632	0.01231	0.03863	
2.8	-3.00	0.1369	-0.1554	0.00648	0.01223	0.01871	
2.9	-1.50	0.3135	-0.1482	0.00934	0.01222	0.02156	
2.10	0.00	0.4862	-0.1401	0.01476	0.01210	0.02686	
2.11	1.50	0.6610	-0.1278	0.02540	0.01177	0.03717	
2.12	-3.00	0.1413	-0.1539	0.00670	0.01272	0.01939	
2.13	-1.50	0.3199	-0.1482	0.00953	0.01272	0.02225	
2.14	0.00	0.4974	-0.1415	0.01517	0.01263	0.02780	
2.15	1.50	0.6776	-0.1308	0.02617	0.01239	0.03855	
2.16	-3.00	0.1252	-0.1578	0.00611	0.01302	0.01913	
2.17	-2.00	0.2408	-0.1534	0.00792	0.01303	0.02094	
2.18	-1.50	0.2969	-0.1513	0.00926	0.01300	0.02226	
2.19	-1.00	0.3556	-0.1492	0.01083	0.01298	0.02381	
2.20	0.00	0.4828	-0.1433	0.01430	0.01287	0.02717	
2.21	1.00	0.6156	-0.1352	0.02011	0.01265	0.03276	
2.22	1.50	0.6733	-0.1314	0.02499	0.01248	0.03748	
2.23	-3.00	0.1449	-0.1575	0.00638	0.01312	0.01950	
2.24	-2.00	0.2658	-0.1537	0.00805	0.01312	0.02117	
2.25	-1.50	0.3258	-0.1519	0.00932	0.01310	0.02242	
2.26	-1.00	0.3851	-0.1500	0.01087	0.01308	0.02395	
2.27	0.00	0.5040	-0.1455	0.01496	0.01299	0.02795	
2.28	1.00	0.6274	-0.1392	0.02137	0.01281	0.03417	
2.29	1.50	0.6890	-0.1356	0.02634	0.01265	0.03899	
2.30	-3.00	0.1014	-0.1728	0.01292	0.01551	0.02843	
2.31	-2.00	0.2133	-0.1643	0.01237	0.01552	0.02789	
2.32	-1.50	0.2703	-0.1606	0.01258	0.01551	0.02809	
2.33	-1.00	0.3196	-0.1567	0.01311	0.01548	0.02858	
2.34	0.00	0.4404	-0.1538	0.01573	0.01538	0.03112	
2.35	1.00	0.5618	-0.1423	0.02095	0.01521	0.03617	dcl<.001,dcd=.0002,dcm<.001
2.36	1.50	0.6221	-0.1355	0.02486	0.01505	0.03992	dcl<.001,dcd=.0003,dcm<.001
2.37	-3.00	0.0935	-0.1645	0.01399	0.01533	0.02932	dcl=.003,dcd=.0007,dcm=.002
2.38	-2.00	0.2019	-0.1544	0.01293	0.01530	0.02823	dcl=.007,dcd=.0005,dcm=.004
2.39	-1.50	0.2425	-0.1519	0.01357	0.01528	0.02885	dcl=.005,dcd=.0004,dcm=.003
2.40	-1.00	0.3044	-0.1437	0.01309	0.01525	0.02833	dcl=.006,dcd=.0004,dcm=.002
2.41	0.00	0.4033	-0.1389	0.01532	0.01515	0.03047	dcl=.007,dcd=.0003,dcm=.002
2.42	1.00	0.5298	-0.1274	0.01985	0.01503	0.03487	dcl=.002,dcd=.0002,dcm=.001
2.43	1.50	0.5962	-0.1218	0.02337	0.01487	0.03824	dcl=.005,dcd=.0005,dcm=.002

Table 6. Force and Moment Results for Case II (continued)

Case	α , deg	C_L	C_{M_y}	C_{D_p}	C_{D_v}	$C_{D_{tot}}$	Notes
2.44	-3.00	0.1213	-0.1658	0.01356	0.01552	0.02909	dcd<.0001
2.45	-2.00	0.2269	-0.1566	0.01321	0.01554	0.02875	dcd<.0001
2.46	-1.50	0.2787	-0.1529	0.01341	0.01552	0.02893	dcd<.0001
2.47	-1.00	0.3306	-0.1488	0.01387	0.01550	0.02937	dcd<.0001
2.48	0.00	0.4277	-0.1401	0.01594	0.01541	0.03135	
2.49	1.00	0.5485	-0.1307	0.02062	0.01523	0.03585	
2.50	1.50	0.6280	-0.1350	0.02408	0.01520	0.03928	
2.51	0.49	0.5592	-0.1436	0.01789	0.01260	0.03050	
2.52	0.49	0.5423	-0.1361	0.01732	0.01203	0.02935	
2.53	0.49	0.5552	-0.1383	0.01776	0.01258	0.03034	
2.54	0.49	0.5501	-0.1395	0.01657	0.01279	0.02936	
2.55	0.49	0.5615	-0.1416	0.01711	0.01278	0.02989	

Table 7. Force and Moment Results for Case III

Case	α , deg	C_L	C_{M_y}	C_{D_p}	C_{D_v}	$C_{D_{tot}}$	Notes
3.1	-0.0090	0.500	-0.1469	0.01516	0.01267	0.02784	
3.2	0.4900	0.500	-0.1488	0.01792	0.01532	0.03324	
3.3	0.1200	0.500	-0.1425	0.01478	0.01286	0.02764	
3.4	0.7600	0.500	-0.1297	0.01849	0.01508	0.03357	dcl=.004,dcd=.0003,dcm=.002
3.5	-0.0331	0.500	-0.1457	0.01479	0.01300	0.02779	
3.6	0.6125	0.500	-0.1347	0.01844	0.01521	0.03364	dcd<.0001